Available online at www.sciencedirect.com

ScienceDirect

journal homepage: www.elsevier.com/locate/he

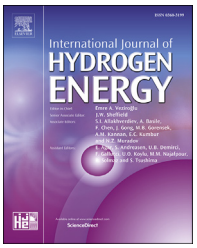

Peptide A4 based AuAg alloyed nanoparticle networks for electrocatalytic reduction of oxygen

Qiannan Wang [a], Hongyu Yang [a], Zhijun Zhou [b,c,**], Likai Wang [a], Wei Yan [a], Wen Wu [a], Shaowei Chen [a,d], Zhen Liu [e,f], Zhenghua Tang [a,g,*]

[a] New Energy Research Institute, School of Environment and Energy, South China University of Technology, Guangzhou Higher Education Mega Centre, Guangzhou, 510006, China

[b] Institute of Nuclear Physics and Chemistry, China Academy of Engineering Physics, 64 Mianshan Road, Mianyang, Sichuan, 621000, China

[c] Collaborative Innovation Center of Radiation Medicine of Jiangsu Higher Education Institute, Soochow University, Suzhou, Jiangsu, China

[d] Department of Chemistry and Biochemistry, University of California, 1156 High Street, Santa Cruz, CA, 95064, United States

[e] Department of Materials Science and Engineering, University of Maryland, College Park, MD, 20742-4111, United States

[f] Department of Physics & Engineering, Frostburg State University, Frostburg, MD, 21532-2303, United States

[g] Guangdong Provincial Key Laboratory of Atmospheric Environment and Pollution Control, Guangdong Provincial Engineering and Technology Research Center for Environmental Risk Prevention and Emergency Disposal, School of Environment and Energy, South China University of Technology, Guangzhou Higher Education Mega Centre, Guangzhou, 510006, China

ARTICLE INFO

Article history:
Received 4 January 2017
Received in revised form
21 February 2017
Accepted 23 February 2017
Available online 15 March 2017

Keywords:
Peptide A4
AuAg alloys
Nanoparticle network
Oxygen electroreduction
Fuel cell

ABSTRACT

Peptide based methods create new revenues to fabricate stable, multifunctional noble metal nanomaterials under mild and green synthesis conditions. Peptide sequence A4 stabilized AuAg alloyed nanomaterials were fabricated through a facile and straightforward approach. The as-prepared alloyed nanomaterials demonstrated effective catalytic activity toward oxygen electroreduction in alkaline media. Both the metal-to-A4 ratio and Au-to-Ag ratio were optimized to enrich the electrocatalytic performance, and the sample of Au:Ag:A4 = 10:30:1 exhibited the highest activity among the series. The performance of Au:Ag:A4 = 10:30:1 is comparable with that of commercial Pt/C, within the context of onset potential, diffusion-limited current density as well as long-term stability. The as-prepared samples were characterized by UV–visible absorbance, transmission electron microscopy (TEM), as well as X-ray photoelectron microscopy (XPS). The improved activity is probably attributed to the alloying induced ensemble effects and electronic effects. This discovery may shed light on fabricating peptide based alloys as highly efficient catalysts with enhanced stability for oxygen reduction reaction (ORR).

* *Corresponding author*. New Energy Research Institute, School of Environment and Energy, South China University of Technology, Guangzhou Higher Education Mega Centre, Guangzhou, 510006, China.

** *Corresponding author*. Institute of Nuclear Physics and Chemistry, China Academy of Engineering Physics, 64 Mianshan Road, Mianyang, Sichuan, 621000, China.

E-mail addresses: zhouzjiang@yeah.net (Z. Zhou), zhht@scut.edu.cn (Z. Tang).

http://dx.doi.org/10.1016/j.ijhydene.2017.02.173

Introduction

Proton exchange membrane fuel cells (PEMFCs) have been attracting numerous research interests in the past decade, mainly thanks to their high energy density, low operation temperature and negligible detrimental environmental impacts [1–4]. Developing high-efficiency electrocatalysts for oxygen reduction reaction (ORR) occurring at the cathode is crucial for large scale commercialization of PEMFCs [5–7]. Typically, platinum-based hybrid materials supported on carbon (20 wt% Pt/C) have been widely regarded as state-of-art catalyst for ORR [8–11]. However, the earth abundance of Pt is quite limited hence the price is very high, and the long-term stability of such Pt/C electrocatalyst is also a remaining challenge [12]. These factors have been the major obstacles that hamper the commercialization of PEMFCs. Consequently, great deals of research efforts have been devoted to developing highly efficient, cost-effective electrocatalysts with enhanced stability for ORR [13–29].

Alloying is one of the most important approaches to fabricate noble metal electrocatalysts for ORR [9]. Exceptional activity and robust stability can be obtained from alloyed metal nanoparticles due to the ensemble and ligand effects [30]. On one hand, compared to Pt, the earth abundance of Au is much higher, while Ag is a comparatively cheaper noble metal in the periodic table. Au alloying with Ag would be a great choice to fabricate noble metal catalysts to significantly lower the cost while maintaining desirable electro-catalytic activity. On the other hand, when exposed to air, Ag surface can be easily oxidized hence a surface ligand is inevitable for improving stability. Moreover, the ligand can act as a template, which plays an important role in nanoparticle formation. Small organic molecules [31], bio-molecules such as protein [32], and dendrimer [33] have been utilized as template for fabricating alloy nanoparticles with well-defined structures. Recently, peptide has emerged as a promising ligand and template to manipulate the synthesis of alloyed noble metal nanoparticles for electrochemical reactions. Peptide-based metal nanomaterials are normally prepared in water at room temperature, and more importantly, peptide sequence with specific binding affinity for target substrate can direct the nuclei growth and nanoparticle formation hence precisely control the size, shape, composition as well as subtle local surface microstructures of noble metal nanomaterials [34,35]. For instances, Bedford et al. successfully showcased the nanoscale surface segregation of AuPd bimetallic nanoparticles, and surface-dependent catalytic activities were observed for methanol oxidation [36]. Recently, through peptide-based self-assembly, Kim group documented the synthesis and catalytic response to oxygen reduction of surface-composition-controlled AuPt bimetallic nanoparticles on carbon nanotubes [37].

Peptide AG4 (Sequence: NPSSLFRYLPSD, abbreviated as A4) was initially selected by incubating silver particles with the combinatorial phage display library. Note that A4 bears strong binding affinity for Ag substrates, and Rajesh et al. demonstrated that it can interact with the nuclei or metal clusters hence accelerated the growth of a particular phase or phases [38]. Interestingly, Baneyx group discovered that, with A4 sequence attached to MBP2 protein, the binding affinity to silver substrate can be amplified at least 1 order of magnitude, and the as-formed Ag nanoparticles were excellent enhancers for Raman spectroscopic surface scattering [39]. Herein, peptide A4 was used as a template to guide and stabilize the AuAg alloyed nanoparticle networks through a facile wet chemical method and the as-prepared alloys demonstrated effective activity toward ORR. By tuning the ratio of metal-to-A4 and the Au/Ag ratio, different performances toward ORR were observed. With the increasing of metal (Au + Ag)-to-peptide ratio, the ORR activity gradually increased, however, further increase of metal loading would decrease the activity. Meanwhile, different Au/Ag ratio also affects the ORR activity significantly. The sample (Au:Ag:A4 = 10:30:1) exhibited the best activity among the series. It also demonstrated markedly higher diffusion-limited current density and long-term stability than the state-of-art commercial Pt/C catalysts.

Materials and methods

Chemicals

Hydrogen tetrachloroauric acid (III) trihydrate ($HAuCl_4 \cdot 3H_2O$, 98%) was obtained from Energy Chemicals (Shanghai, China), Peptide A4 (purity: >95%) was purchased from Top-Peptide (Shanghai, China), with purity confirmed by high performance liquid chromatographic (HPLC) and mass spectrometric (MS) analysis. Sodium borohydride ($NaBH_4$, 98%) was purchased from Aladdin industrial Corporation (Shanghai, China). Silver nitrate ($AgNO_3$, 99%) and Pt/C (20 wt %) were obtained from Alfa Aesar. Water was supplied with a Barnstead nanopure water system (18.3 MΩ cm). All chemicals were used as received without further purification.

Synthesis of peptide based nanomaterials

The synthesis of Au:Ag:A4 = X:X:1 (X is the molar ratio of Au or Ag to A4, X = 10, 15, 20, 25) was conducted by following a modified procedure in previous reports in our group [40,41]. For the synthesis of Au:Ag:A4 = 10:10:1, a typical procedure can be described as follows: 0.5 mL A4 solution (1 mM), 50 μL $AgNO_3$ solution (0.1 M) and 125 μL $HAuCl_4$ (40 mM) were first mixed and added into 2.025 mL H_2O. The mixture was stirred until yellow particles appeared (~15 min), then 300 μL freshly prepared $NaBH_4$ (0.1 M) aqueous solution was added rapidly with a slight shaking. The solution turned from yellow to black immediately and was kept stewing at last 1 h at room temperature. After centrifugation, the black particles were collected and then washed by water three times, and further dried in air overnight. The solids were subjected to further characterization and electrochemical tests. As the metal-to-peptide molar ratio is 20:1, the sample was denoted as Au:Ag:A4 = 10:10:1. The samples of Au:Ag:A4 = 15:15:1, Au:Ag:A4 = 20:20:1, and Au:Ag:A4 = 25:25:1 were prepared in a similar manner, but the volume of A4 solution was changed into 0.33 mL, 0.25 mL, and 0.2 mL respectively, while the total volume of the reaction solution was kept 3 mL. For all the above samples, the molar ratio of Au-to-Ag was kept as 1:1.

While to optimize the Au:Ag ratio, other samples with different Au-to-Ag molar ratios were also synthesized. The

samples of Au:Ag:A4 = 0:40:1, Au:Ag:A4 = 10:30:1, Au:Ag:A4 = 20:20:1, Au:Ag:A4 = 30:10:1, and Au:Ag:A4 = 40:0:1 were prepared in a similar protocol, while the total volume was kept 3 mL and the A4 concentration was kept constant. The $AgNO_3$ solution (0.1 M) and $HAuCl_4$ (40 mM) with different volumes were added to control the molar ratios of Au-to-Ag were 0:40, 10:30, 20:20, 30:10, and 40:0.

Characterizations

The surface chemical composition of the samples was probed by X-ray photoelectron spectroscopy (XPS) by a VG Multi Lab 2000 instrument with a monochromatic Al Kα X-ray source (Thermo VG Scientific). Absorbance spectra were acquired with a Shimadzu 2600/2700 UV–visible scanning spectrophotometer. The morphology and microstructures of the samples were observed by a high-resolution transmission electron microscope (JEOL TEM-2010) equipped with an energy dispersive X-ray spectroscopy (EDS) system.

Electrochemical measurements

The electrochemical tests were conducted by a three-electrode system, in which a glassy carbon-disk working electrode (diameter 5.61 mm, Pine Instrument Inc., RRDE collection efficiency is 37%) and a AgCl/Ag and a platinum wire was employed as both reference electrode and counter electrode. The working electrode was cleaned by polishing with aqueous slurries of 0.3 μm alumina powders on a microcloth. 2 mg of a catalyst was dispersed in 1.0 mL ethanol solution containing 10 μL Nafion (5 wt%, Aldrich), and the dispersion was then sonicated for at last 30 min to prepare a catalyst ink. Typically, 10 μL of the ink was dropcast onto the glassy carbon disk and dried at room temperature. For all catalyst samples and Pt/C, the loading was calculated as 80.8 μg cm^{-2}. All the cyclic voltammograms (CV) were acquired at a scan rate of 10 mV s^{-1}, and the linear sweep voltammograms (LSV) were collected in oxygen-saturated 0.1 M KOH solution at a scan rate of 10 mV s^{-1} with different rotation rates from 100 to 2500 rpm, the disk potential ranged from −0.04 V to +1.16 V while the ring potential was set as +0.5 V during the measurement. The durability and stability of the catalysts were examined by chronoamperometric measurements at +0.5 V for 40,000 s in an oxygen-saturated 0.1 M KOH solution. The rotation rate was 900 rpm. The Ag/AgCl reference electrode was calibrated with a reversible hydrogen electrode (RHE), which was performed in a high-purity H_2 (99.999%) saturated electrolyte with a Pt wire as both the working electrode and counter electrode. In 0.1 M KOH, $E_{RHE} = E_{Ag/AgCl} + 0.966$ V.

Results and discussions

ORR activity comparison of the (Au + Ag):A4 = X:1 (X is controlled as 20, 30, 40 and 50, while Au-to-Ag ratio fixed as 1)

To start with, a series of peptide stabilized AuAg nanomaterials were first fabricated. As both the metal (Au + Ag)-to-peptide ratio and the ratio of Au-to-Ag will affect the ORR activity, initially, we synthesized a series of samples with Au-to-Ag ratio fixed as 1 while the ratio of metal-to-peptide were varied. Fig. 1 depicts the electrochemical performance of the samples with the molar ratio of Au-to-Ag = 1:1, while the ratio of metal (Au + Ag)-to-A4 was controlled as 20, 30, 40 and 50. One can see that, the cathodic peak potential of Au:Ag:A4 = 20:20:1 was more positive than the other samples (Fig. 1a). Notably, the onset potential and diffusion-limited current density increased with the increasing of metal ratio, however, when the ratio of metal (Au + Ag)-to-A4 reached 50, the catalytic activity upon ORR decreased significantly (Fig. 1b). Compared with the other samples in the series, the sample of Au:Ag:A4 = 20:20:1 also exhibited the largest diffusion-limited current density (4.46 mA cm^{-2} at 1600 rpm), as summarized in Table S1. These results suggest that a metal-to-A4 ratio of 40 would result in better ORR activity than other ratios.

ORR activity comparison of the samples with different Au-to-Ag ratio and same metal-to-peptide ratio (40:1)

Since the sample of metal-to-A4 (40:1) demonstrated the most prominent ORR activity, subsequently, a series of samples with metal-to-peptide ratio fixed as 40:1 and different Au-to-Ag ratios were fabricated and subjected for ORR test. From Fig. 2a, it is observable that the samples with different Au-to-Ag ratios exhibited rather distinctive ORR activity. The sample of Au/Ag = 10:30 demonstrated the most positive cathodic peak potential and largest cathodic peak current density. Consistent results were also obtained from the LSV measurements. As shown in Fig. 2b, the sample of Au/Ag = 10:30 exhibited an onset potential of 0.94 V and a diffusion-limited current density of 4.87 mA cm^{-2}, both of them were superior than the other samples in the series. It is worth noting that the onset potential of the sample Au/Ag = 10:30 (at 0.94 V) is slightly lower than that of Pt/C (at 0.98 V), however, the diffusion-limited current density at +0.40 V and 1600 rpm of the sample (4.87 mA cm^{-2}) exhibited a greater value than Pt/C (4.67 mA cm^{-2}) with the same catalyst loading. Combined with all the above findings, the sample of Au/Ag = 10:30 and metal-to-A4 = 40:1 exhibited the best activity upon ORR in the series.

Based on the RRDE data (Fig. 2b), the number of electron transfer (n) and the H_2O_2 yield in ORR can be calculated through the equations of

$$n = \frac{4I_d}{I_r/N + I_d} \quad (1)$$

$$H_2O_2\% = \frac{200I_r/N}{I_r/N + I_d} \quad (2)$$

where I_d is the disk current, I_r is the ring current, and N is the RRDE collection efficiency (0.37). The calculated results can be found in Fig. 2c, and the n values of the samples in the potential range of 0 to +0.80 V were summarized in Table S2. As listed in Table S2, for the sample of Au:Ag:A4 = 40:0:1 and 0:40:1, the electron transfer number is 3.18–3.70 and 3.34–3.76, respectively. The n values of the alloyed samples are much higher, approximately in the range of 3.80–3.98. Correspondingly, the sample of Au:Ag:1 = 40:0:1 and 0:40:1

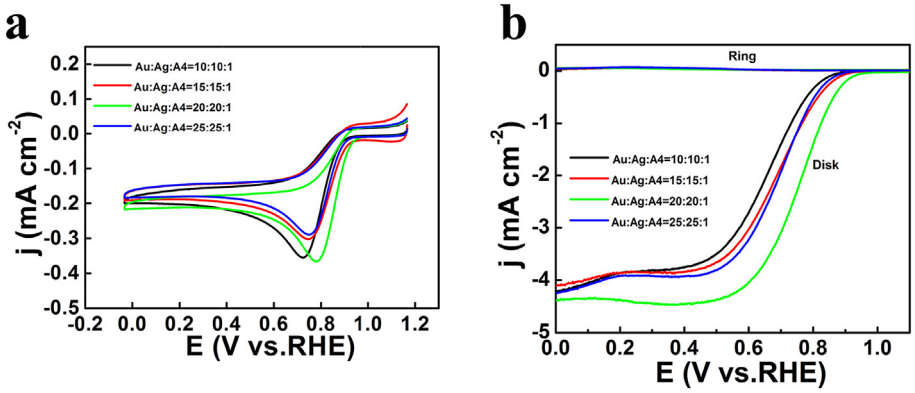

Fig. 1 – The electrochemical performance of the glassy carbon electrode (GCE) modified with the samples (Au:Ag:A4 = X:X:1, X = 10, 15, 20 or 25) in O_2-saturated 0.1 M KOH solution: (a) Cyclic and (b) Rotating disk electrode (RDE) voltammograms at a rotation speed of 1600 rpm with a 10 mV/s potential sweep rate. The catalyst loading is 80.8 μg/cm^2.

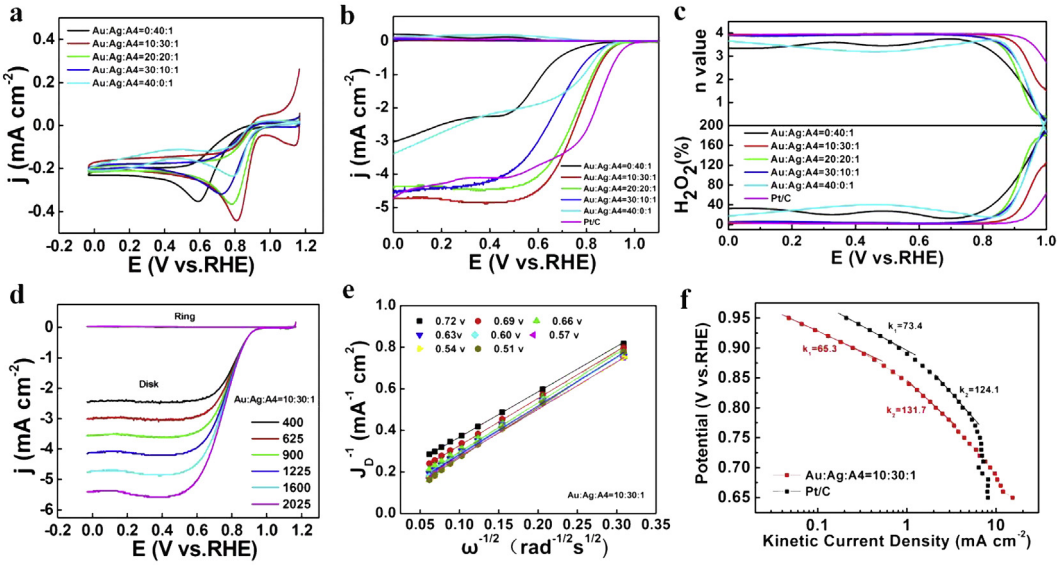

Fig. 2 – The electrochemical performance of the glassy carbon electrode (GCE) modified with the samples of different Au-to-Ag ratio and same metal-to-peptide ratio (40:1) and Pt/C in O_2-saturated 0.1 M KOH solution: (a) Cyclic and (b) Rotating disk electrode (RDE) voltammograms at a rotation speed of 1600 rpm with 10 mV/s potential sweep rate, (c) Plots of number of electron transfer and H_2O_2 (%) yield, (d) Voltammetric current of Au:Ag:A4 = 10:30:1 at the rotation rate of 400–2025 rpm with 10 mV/s potential sweep rate, (e) Corresponding Koutecky–Levich plots of Au:Ag:A4 = 10:30:1 catalyst at different potentials, (f) The corresponding Tafel plots of Au:Ag:A4 = 10:30:1 and commercial Pt/C. All measurements were conducted with a catalyst loading of 80.8 μg cm^{-2} in an O_2-saturated 0.1 M KOH aqueous solution at a potential scan rate of 10 mV s^{-1}.

possessed relatively high yield of H_2O_2, both of them are larger than 10% and can reach 40% even higher at certain potential. For all the alloyed samples, the yield of H_2O_2 is less than 10%. Such high electron transfer number and quite low H_2O_2 yield indicate that the alloyed samples can catalyze oxygen reduction very efficiently. It is worth noting that, the sample of Au:Ag:A4 = 10:30:1 possessed the highest electron transfer number (3.94–3.98), which is close to Pt/C (n = 3.92–3.98) within the wide potential range of +0.20 to +0.80 V, meanwhile, the H_2O_2 yield for Au:Ag:A4 = 10:30:1 was 1.47–3.58 (%), also comparable with Pt/C (1.42–4.73%) in the potential range of 0–0.8 V. Taking together, these results indicated that, the ORR activity of Au:Ag:A4 = 10:30:1 was close or comparable to commercial Pt/C. Fig. 2d depicted that the voltammetric currents of Au:Ag:A4 = 10:30:1 increased with the increasing of the electrode rotation rate.

The electrocatalytic activity of the Au:Ag:A4 = 10:30:1 sample for ORR was further examined and compared with commercial Pt/C by voltammetric measurements. As shown in Fig. S1, in CV measurements, there is no redox peak (black dash curves) within the potential range of −0.04 V to +1.16 V when the electrode modified by the sample or Pt/C were immersed in N_2-saturated 0.1 M KOH solution. Nevertheless, well-defined voltammetric peak at 0.81 V (for Au:Ag:A4 = 10:30:1) or at

0.8 V (for Pt/C) can be readily identified in oxygen-saturated 0.1 M KOH solution, indicating effective activity of both catalysts for oxygen reduction. Furthermore, the corresponding Koutecky–Levich (K–L) plots of Au:Ag:A4 = 10:30:1 (Fig. 2e) exhibited a good linearity with a nearly identical slope in the potential range from +0.50 V to 0.75 V. Fig. 2f displays the corresponding Tafel plots of Au:Ag:A4 = 10:30:1 and Pt/C, and the K–L plots and Tafel plots of the other alloyed samples can be found in Fig. S2. The Tafel slopes are typically found at 60 or 120 mV dec^{-1} for the ORR, where the former value corresponds to a pseudo-two-electron reaction as the rate-determining step [22,42] and the latter suggests that the rate-determining step is a first-electron reduction of oxygen, and the subsequent reduction and O–O bond-breaking steps are relatively facile [43]. The Tafel slopes in the present study were calculated as 111.5 mV dec^{-1} for Au:Ag:A4 = 0:40:1, 65.3 mV dec^{-1} for Au:Ag:A4 = 10:30:1, 68.3 mV dec^{-1} for Au:Ag:A4 = 20:20:1, 61.4 mV dec^{-1} for Au:Ag:A4 = 30:10:1, 70 mV dec^{-1} for Au:Ag:A4 = 40:0:1 and 73.4 mV dec^{-1} for Pt/C, respectively, in a low overpotential regime (E > +0.89 V). For most of the alloy samples, the Tafel slope is in the range from 61.4 mV dec^{-1} to 70 mV dec^{-1}, close to that of Pt/C, indicating the reaction mechanism of ORR on the surface of these catalysts were similar with that of Pt/C, that is, the ORR reaction probably is a pseudo-two-electron reduction step. Meanwhile, the Tafel slope at the potential below +0.85 V, was calculated as 175.4 mV dec^{-1} for Au:Ag:A4 = 0:40:1, 131.7 mV dec^{-1} for Au:Ag:A4 = 10:30:1, 118.1 mV dec^{-1} for Au:Ag:A4 = 20:20:1, 138.4 mV dec^{-1} for Au:Ag:A4 = 30:10:1, 138.5 mV dec^{-1} for Au:Ag:A4 = 40:0:1 and 124.1 mV dec^{-1} for Pt/C, indicating that the reaction rate was probably limited by the first electron transfer to oxygen molecules [3,5,6,22].

Absorbance of Au:Ag-X samples with different Au-to-Ag ratios

Meanwhile, the optical property and surface structure of the as-prepared alloyed nanomaterials were tested and observed. The UV–visible absorbance spectra of the samples are shown in Fig. 3. One can see that, with the increasing of the Au content, the absorbance peak at ~300 nm becomes more prominent, while the absorbance peak at ~400 nm weakened with the decreasing of Ag content. Such absorbance feature is probably attributed to the peptide-metal interaction [44].

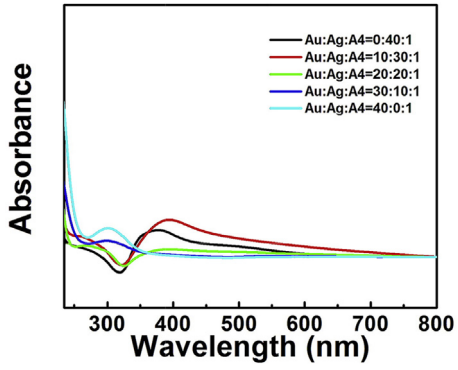

Fig. 3 – UV–visible absorption spectra of Au:Ag-X samples (Metal (Au + Ag):A4 = 40:1) with different Au-to-Ag ratios.

TEM analysis of the sample of Au:Ag:A4 = 10:30:1

The morphology and elemental distribution of Au:Ag:A4 = 10:30:1 are shown in Fig. 4. From Fig. 4a and b, intercrossed nanoparticle networks can be observed for the sample of Au:Ag:A4 = 10:30:1. As a note, such well-defined intriguing structure has been reported in a recent study [45]. Further EDX analysis (Fig. 4c) revealed the atomic Au-to-Ag ratio of 64.2/35.8 in the sample. Note that, the initial loading molar ratio of Au-to-Ag during the synthesis was 10:30. Such difference is probably caused by the technique details, as EDS spectroscopy can only measure the elemental distribution in an extremely small region but not the whole target [46,47]. The representative TEM images of the other samples with different ratios of Au-to-Ag are shown in Fig. S3. Interestingly, well-defined spherical particles (Figs. S3a and d) were obtained when only Ag or Au existed alone with A4. For the samples of Au:Ag:A4 = 20:20:1 and Au:Ag:A4 = 30:10:1, the nanoparticle networks were less distinctive than Au:Ag:A4 = 10:30:1. With the increasing of gold mass, more aggregates and bulky materials can be clearly observed. As peptide A4 bears specific binding affinity to Ag, the decreasing of Ag contents and increasing of Au contents may strengthen the metal–metal interaction, hence facilitate the formation of bulky structured materials or aggregates.

XPS analysis of Au:Ag:A4 samples with different Au-to-Ag ratios

The electronic structures of these alloyed nanomaterials were next examined by XPS measurements [48,49]. The XPS scan spectra of the Au:Ag:A4 = 10:30:1 (Fig. 5) sample first confirm the co-existence of both Au and Ag elements. From the XPS survey scan spectra (Fig. 5a), the molar elemental ratio of Au-to-Ag was estimated as 0.75:2.43, which is close with the initial loading molar ratio of Au-to-Ag (1:3). The high-resolution XPS focus scan spectra of Au4f and Ag3d electrons are shown in Fig. 5b and c, respectively. The binding energy of Au4f7/2 electrons of all the alloyed samples is in the between of Au(I) (~84.7 eV) and bulk gold (~83.5 eV) [50,51] while similarly, the binding energy of Ag3d5/2 electrons is in the range of Ag(I) (~369.4 eV) and Ag(0) (~367.0 eV) [52]. One may notice that, the binding energy of Au4f7/2 electrons decreased from 84.1 eV for Au:Ag:A4 = 40:0:1 (No Ag) to 83.7 eV for Au:Ag:A4 = 10:30:1 with the decreasing of Au ratio (increasing of Ag ratio) in alloys (Fig. 5b). Correspondingly, the binding energy of Ag3d5/2 electrons increased from 367 eV for Au:Ag:A4 = 0:40:1 (No Au) to 368.1 eV for Au:Ag:A4 = 30:10:1 with the decreasing of Ag ratio (increasing of Au ratio) in alloys (Fig. 5c). The decreased Au4f7/2 binding energies and increased Ag3d5/2 binding energies can be probably attributed to the electron donation from the less electronegative Ag heteroatoms (χ = 1.9) to the more electronegative Au atoms (χ = 2.4) [53].

Durability comparison of Au:Ag:A4 = 10:30:1 and commercial Pt/C for ORR

Finally, the chronoamperometric measurements were carried out to compare the long-term durability of Au:Ag:A4 = 10:30:1 with commercial Pt/C for ORR. As depicted in Fig. 6, after more than 10 h's continuous operation, the cathodic current of the

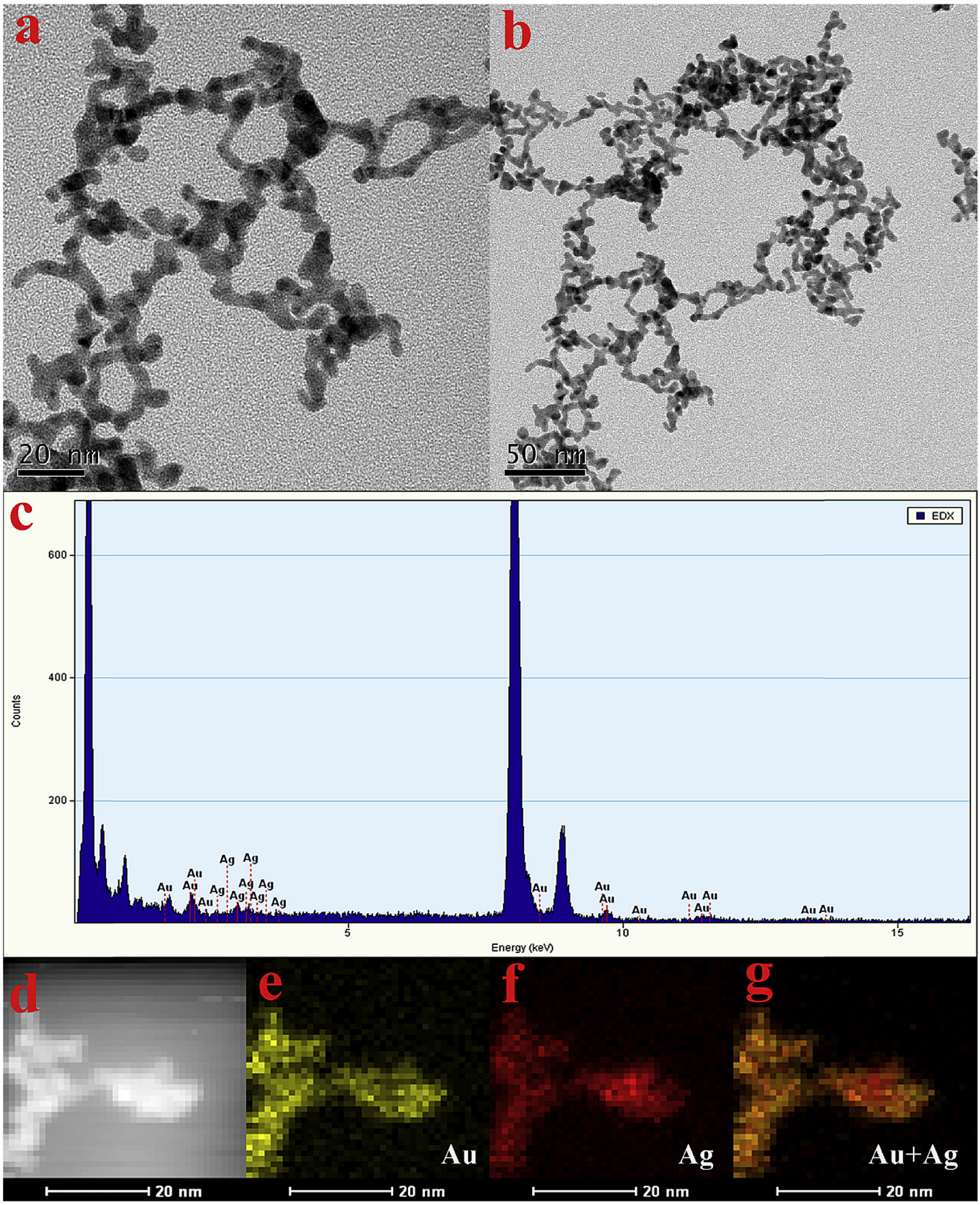

Fig. 4 – Morphology and structure characterization of Au:Ag:A4 = 10:30:1. Typical HR-TEM images at 20 nm (a) and 50 nm magnification (b). (c) Representative TEM-EDX images. (d) HAADF-STEM elemental mapping images of Au (e), Ag (f) and Au + Ag (g).

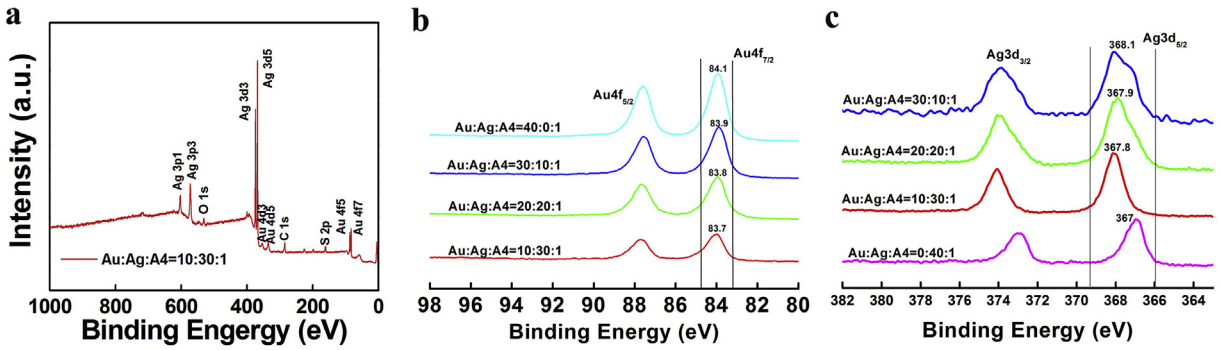

Fig. 5 – XPS survey scan spectra of Au:Ag:A4 = 10:30:1 (a), Au4f (b) and Ag3d (c) electrons of alloyed nanoparticles with different Au:Ag ratios (0/40, 10/30, 20/20, 30/10, 40/0).

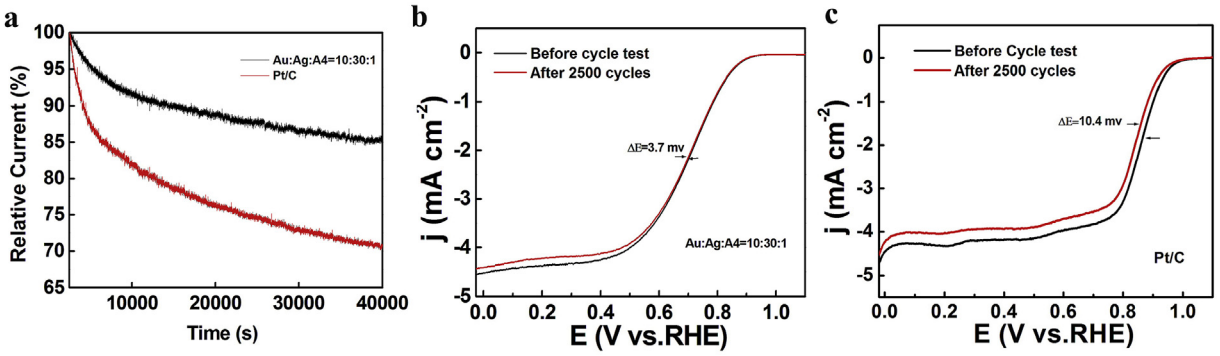

Fig. 6 – (a) Chronoamperometric responses for ORR at Au:Ag:A4 = 10:30:1 and Pt/C electrodes in an O_2-saturated 0.1 M KOH solution at +0.5 V for 40, 000 s. The accelerated durability tests (ADT) of Au:Ag:A4 = 10:30:1 (b) and commercial Pt/C (c) were carried out by before and after 2500 cycles between 0.6 and 1.0 V at a scan rate of 50 mV s^{-1} with a rotation speed of 1600 rpm in an O_2-saturated 0.1 M KOH solution.

Au:Ag:A4 = 10:30:1 retained about 85% of its initial current, while commercial Pt/C catalyst exhibited a clear loss of 35% of the initial value under the same experimental conditions. This suggests that the stability of Au:Ag:A4 = 10:30:1 is remarkably higher than Pt/C. To further assess the durability of the catalysts, accelerated durability tests were carried out by cycling the catalyst over the potential range from +0.6 to 1.0 V at 50 mV s^{-1} in an O_2-saturated 0.1 M KOH solution. As presented in Fig. 6b, the half-wave potential of Au:Ag:A4 = 10:30:1 shifted negatively by only 3.7 mV after 2500 cycles test, while commercial Pt/C displayed a much bigger negative shift of 10.4 mV (Fig. 6c), further attesting the higher durability of Au:Ag:A4 = 10:30:1 than commercial Pt/C. The enhanced long-term stability might be attributed to the following factors:1. The strong electronic interaction between Au and Ag atoms induced synergistic effects, which are favorable for the kinetics of ORR [46,54]; 2. Peptide A4 serves as the protecting agent, which prevents the strong metal–metal interaction for coalescence and/or aggregation [38].

Conclusions

Peptide A4 based AuAg alloyed nanoparticle networks were developed and discovered as efficient electrocatalysts for ORR in alkaline media. The sample of Au:Ag:A4 = 10:30:1 exhibited the top activity for ORR among a series of sample. Its performance was comparable to that of commercial Pt/C, evidenced by an onset potential at +0.94 V vs RHE, high electron transfer number of 3.94–3.98 and very low H_2O_2 yield, as well as larger diffusion-limited current density compared with Pt/C. Furthermore, its long-term durability was remarkably higher than commercial Pt/C. This finding is able to further power the rational design of peptide templated alloyed noble metal nanoparticle networks with desirable electrocatalytic activities for fuel cell applications and beyond.

Acknowledgements

This work was supported by the National Natural Science Foundation of China (No. 21501059). Z.H.T also acknowledges financial support from Project of Public Interest Research and Capacity Building of Guangdong Province (No. 2015A010105009), Guangdong Innovative and Entrepreneurial Research Team Program (No. 2014ZT05N200), and Guangdong Natural Science Funds for Distinguished Young Scholars (No. 2015A030306006).

Appendix A. Supplementary data

Supplementary data related to this article can be found at http://dx.doi.org/10.1016/j.ijhydene.2017.02.173.

REFERENCES

[1] Debe MK. Electrocatalyst approaches and challenges for automotive fuel cells. Nature 2012;486:43–51.
[2] Kraytsberg A, Ein-Eli Y. Review of advanced materials for proton exchange membrane fuel cells. Energy Fuels 2014;28:7303–30.
[3] Liu M, Zhang R, Chen W. Graphene-supported nanoelectrocatalysts for fuel cells: synthesis, properties, and applications. Chem Rev 2014;114:5117–60.
[4] Peighambardoust SJ, Rowshanzamir S, Amjadi M. Review of the proton exchange membranes for fuel cell applications. Int J Hydrogen Energy 2010;35:9349–84.
[5] Cui C-H, Yu S-H. Engineering interface and surface of noble metal nanoparticle nanotubes toward enhanced catalytic activity for fuel cell applications. Acc Chem Res 2013;46:1427–37.
[6] Jiao Y, Zheng Y, Jaroniec M, Qiao SZ. Design of electrocatalysts for oxygen- and hydrogen-involving energy conversion reactions. Chem Soc Rev 2015;44:2060–86.
[7] Wong WY, Daud WRW, Mohamad AB, Kadhum AAH, Loh KS, Majlan EH. Recent progress in nitrogen-doped carbon and its composites as electrocatalysts for fuel cell applications. Int J Hydrogen Energy 2013;38:9370–86.
[8] Guo S, Zhang S, Sun S. Tuning nanoparticle catalysis for the oxygen reduction reaction. Angew Chem Int Ed 2013;52:8526–44.
[9] Wang C, Markovic NM, Stamenkovic VR. Advanced platinum alloy electrocatalysts for the oxygen reduction reaction. ACS Catal 2012;2:891–8.
[10] Capelo A, Esteves MA, de Sá AI, Silva RA, Cangueiro L, Almeida A, et al. Stability and durability under potential cycling of Pt/C catalyst with new surface-functionalized carbon support. Int J Hydrogen Energy 2016;41:12962–75.
[11] Wang L, Tang Z, Yan W, Wang Q, Yang H, Chen S. Co@Pt Core@Shell nanoparticles encapsulated in porous carbon derived from zeolitic imidazolate framework 67 for oxygen electroreduction in alkaline media. J Power Sources 2017;343:458–66.
[12] Puthusseri D, Ramaprabhu S. Oxygen reduction reaction activity of platinum nanoparticles decorated nitrogen doped carbon in proton exchange membrane fuel cell under real operating conditions. Int J Hydrogen Energy 2016;41:13163–70.
[13] Liang H-W, Wei W, Wu Z-S, Feng X, Müllen K. Mesoporous metal–nitrogen-doped carbon electrocatalysts for highly efficient oxygen reduction reaction. J Am Chem Soc 2013;135:16002–5.
[14] Niu W, Li L, Liu X, Wang N, Liu J, Zhou W, et al. Mesoporous N-doped carbons prepared with thermally removable nanoparticle templates: an efficient electrocatalyst for oxygen reduction reaction. J Am Chem Soc 2015;137:5555–62.
[15] Ding W, Li L, Xiong K, Wang Y, Li W, Nie Y, et al. Shape fixing via salt recrystallization: a morphology-controlled approach to convert nanostructured polymer to carbon nanomaterial as a highly active catalyst for oxygen reduction reaction. J Am Chem Soc 2015;137:5414–20.
[16] Wu G, Wang J, Ding W, Nie Y, Li L, Qi X, et al. A strategy to promote the electrocatalytic activity of spinels for oxygen reduction by structure reversal. Angew Chem Int Ed 2016;55:1340–4.
[17] Liu S, Tian N, Xie A-Y, Du J-H, Xiao J, Liu L, et al. Electrochemically seed-mediated synthesis of sub-10 nm tetrahexahedral Pt nanocrystals supported on graphene with improved catalytic performance. J Am Chem Soc 2016;138:5753–6.
[18] Chen Y-Z, Wang C, Wu Z-Y, Xiong Y, Xu Q, Yu S-H, et al. From bimetallic metal-organic framework to porous carbon: high surface area and multicomponent active dopants for excellent electrocatalysis. Adv Mater 2015;27:5010–6.
[19] Zhou M, Wang H-L, Guo S. Towards high-efficiency nanoelectrocatalysts for oxygen reduction through engineering advanced carbon nanomaterials. Chem Soc Rev 2016;45:1273–307.
[20] Bu L, Zhang N, Guo S, Zhang X, Li J, Yao J, et al. Biaxially strained PtPb/Pt core/shell nanoplate boosts oxygen reduction catalysis. Science 2016;354:1410–4.
[21] Wang Q, Wang L, Tang Z, Wang F, Yan W, Yang H, et al. Oxygen reduction catalyzed by gold nanoclusters supported on carbon nanosheets. Nanoscale 2016;8:6629–35.
[22] Wang L, Tang Z, Yan W, Yang H, Wang Q, Chen S. Porous carbon-supported gold nanoparticles for oxygen reduction reaction: effects of nanoparticle size. ACS Appl Mater. Interfaces 2016;8:20635–41.
[23] Sweeney SW, Roseman G, Deming CP, Wang N, Nguyen TA, Millhauser GL, et al. Impacts of oxygen vacancies on the electrocatalytic activity of AuTiO2 nanocomposites towards oxygen reduction. Int J Hydrogen Energy 2016;41:18005–14.
[24] Wang Y, He Q, Ding K, Wei H, Guo J, Wang Q, et al. Multiwalled carbon nanotubes composited with palladium nanocatalysts for highly efficient ethanol oxidation. J Electrochem Soc 2015;162:F755–63.
[25] Wang Y, He Q, Guo J, Wang J, Luo Z, Shen TD, et al. Ultrafine FePd nanoalloys decorated multiwalled cabon nanotubes toward enhanced ethanol oxidation reaction. ACS Appl Mater Interfaces 2015;7:23920–31.
[26] Wang Y, Clancey J, Lu G, Liu J, Liu L, Chaudhuri J, et al. Enhanced methanol oxidation with annealed atomic layer deposited platinum nanoparticles on carbon nanotubes. J Electrochem Soc 2016;163:F1–10.
[27] Choi W, Yang G, Kim SL, Liu P, Sue H-J, Yu C. One-step synthesis of nitrogen-iron coordinated carbon nanotube catalysts for oxygen reduction reaction. J Power Sources 2016;313:128–33.
[28] Yan W, Tang Z, Wang L, Wang Q, Yang H, Chen S. PdAu alloyed clusters supported by carbon nanosheets as efficient electrocatalysts for oxygen reduction. Int J Hydrogen Energy 2017;42:218–27.
[29] Cao L, Lin Z, Huang J, Yu X, Wu X, Zhang B, et al. Nitrogen doped amorphous carbon as metal free electrocatalyst for oxygen reduction reaction. Int J Hydrogen Energy 2017;42:876–85.
[30] Gao F, Goodman DW. Pd-Au bimetallic catalysts: understanding alloy effects from planar models and (supported) nanoparticles. Chem Soc Rev 2012;41:8009–20.
[31] Wang C, Peng S, Chan R, Sun S. Synthesis of AuAg alloy nanoparticles from core/shell-structured Ag/Au. Small 2009;5:567–70.
[32] Mohanty JS, Xavier PL, Chaudhari K, Bootharaju MS, Goswami N, Pal SK, et al. Luminescent, bimetallic AuAg alloy quantum clusters in protein templates. Nanoscale 2012;4:4255–62.
[33] Anderson RM, Yancey DF, Zhang L, Chill ST, Henkelman G, Crooks RM. A theoretical and experimental approach for correlating nanoparticle structure and electrocatalytic activity. Acc Chem Res 2015;48:1351–7.

[34] Dickerson MB, Sandhage KH, Naik RR. Protein- and peptide-directed syntheses of inorganic materials. Chem Rev 2008;108:4935–78.
[35] Briggs BD, Knecht MR. Nanotechnology meets biology: peptide-based methods for the fabrication of functional materials. J Phys Chem Lett 2012;3:405–18.
[36] Bedford NM, Showalter AR, Woehl TJ, Hughes ZE, Lee S, Reinhart B, et al. Peptide-directed PdAu nanoscale surface segregation: toward controlled bimetallic architecture for catalytic materials. ACS Nano 2016;10:8645–59.
[37] Ko Y-S, Kim Y-T, Kim J-H, Kim DH, Kim K-H, Yun WS, et al. Peptide-based bimetallic nanostructures with tailored surface compositions and their oxygen electroreduction activities. CrystEngComm 2016;18:6024–8.
[38] Naik RR, Stringer SJ, Agarwal G, Jones SE, Stone MO. Biomimetic synthesis and patterning of silver nanoparticles. Nat Mater 2002;1:169–72.
[39] Sengupta A, Thai CK, Sastry MSR, Matthaei JF, Schwartz DT, Davis EJ, et al. A genetic approach for controlling the binding and orientation of proteins on nanoparticles. Langmuir 2008;24:2000–8.
[40] Wang Q, Tang Z, Wang L, Yang H, Yan W, Chen S. Morphology control and electro catalytic activity towards oxygen reduction of peptide-templated metal nanomaterials: a comparison between Au and Pt. ChemistrySelect 2016;1:6044–52.
[41] Yang H, Tang Z, Wang L, Zhou W, Li L, Zhang Y, et al. The reactivity study of peptide A3-capped gold and silver nanoparticles with heavy metal ions. Mater Sci Eng B 2016;210:37–42.
[42] He G, Song Y, Liu K, Walter A, Chen S, Chen S. Oxygen reduction catalyzed by platinum nanoparticles supported on graphene quantum dots. ACS Catal 2013;3:831–8.
[43] Liu X, Li L, Zhou W, Zhou Y, Niu W, Chen S. High-performance electrocatalysts for oxygen reduction based on nitrogen-doped porous carbon from hydrothermal treatment of glucose and dicyandiamide. ChemElectroChem 2015;2:803–10.
[44] Palafox-Hernandez JP, Tang Z, Hughes ZE, Li Y, Swihart MT, Prasad PN, et al. Comparative study of materials-binding peptide interactions with gold and silver surfaces and nanostructures: a thermodynamic basis for biological selectivity of inorganic materials. Chem Mater 2014;26:4960–9.
[45] Feng Y, Bu L, Guo S, Guo J, Huang X. 3D platinum–lead nanowire networks as highly efficient ethylene glycol oxidation electrocatalysts. Small 2016;12:4464–70.
[46] Chen H, Fan X, Ma J, Zhang G, Zhang F, Li Y. Green route for microwave-assisted preparation of AuAg-alloy-decorated graphene hybrids with superior 4-NP reduction catalytic activity. Ind Eng Chem Res 2014;53:17976–80.
[47] Gu J, Meng X, Tang Y, Li Y, Zhuang Q, Kong J. Hexagonal boron nitride/polymethyl-vinyl siloxane rubber dielectric thermally conductive composites with ideal thermal stabilities. Compos A Appl Sci Manuf 2017;92:27–32.
[48] Niu W, Li L, Liu X, Zhou W, Li W, Lu J, et al. One-pot synthesis of graphene/carbon nanospheres/graphene sandwich supported Pt3Ni nanoparticles with enhanced electrocatalytic activity in methanol oxidation. Int J Hydrogen Energy 2015;40:5106–14.
[49] Gu J, Yang X, Li C, Kou K. Synthesis of cyanate ester microcapsules via solvent evaporation technique and its application in epoxy resins as a healing agent. Ind Eng Chem Res 2016;55:10941–6.
[50] Tang Z, Xu B, Wu B, Germann MW, Wang G. Synthesis and structural determination of multidentate 2,3-dithiol-stabilized Au clusters. J Am Chem Soc 2010;132:3367–74.
[51] Zhang P. X-ray spectroscopy of gold–thiolate nanoclusters. J Phys Chem C 2014;118:25291–9.
[52] Udayabhaskararao T, Sun Y, Goswami N, Pal SK, Balasubramanian K, Pradeep T. Ag7Au6: a 13-atom alloy quantum cluster. Angew Chem Int Ed 2012;51:2155–9.
[53] Yao H, Kobayashi R, Nonoguchi Y. Enhanced chiroptical activity in glutathione-protected bimetallic (AuAg)18 nanoclusters with almost intact core–shell configuration. J Phys Chem C 2016;120:1284–92.
[54] Chen H-C, Chou S-W, Tseng W-H, Chen IWP, Liu C-C, Liu C, et al. Large AuAg alloy nanoparticles synthesized in organic media using a one-pot reaction: their applications for high-performance bulk heterojunction solar cells. Adv Func Mater 2012;22:3975–84.